

# Suspicious-region segmentation from breast thermogram using DLPE-based level set method

Sourav Pramanik\*, Student Member, IEEE, Debapriya Banik, Debotosh Bhattacharjee, Senior Member, IEEE, Mita Nasipuri, Senior Member, IEEE, Mrinal Kanti Bhowmik, Member, IEEE, and Gautam Majumdar

**Abstract**—Segmentation of suspicious regions (SRs) of a thermal breast image (TBI) is a very significant and challenging problem for identification of breast cancer. Therefore, in this work, we have proposed an active contour model for the segmentation of the SRs in a TBI. The proposed segmentation method combines three significant steps. First, a novel method, called smaller-peaks corresponding to the high-intensity-pixels and the centroid-knowledge of SRs (SCH-CS), is proposed to approximately locate the SRs, whose contours are later used as the initial evolving curves of the level set method (LSM). Second, a new energy functional, called different local priorities embedded (DLPE), is proposed regarding the level set function. DLPE is then minimized using the interleaved level set evolution to segment the potential SRs in a TBI more accurately. Finally, a new stopping criterion is incorporated into the proposed LSM. The proposed LSM not only increases the segmentation speed but also ameliorates the segmentation accuracy. Performance of our SR segmentation method was evaluated on two TBI databases, namely, DMR-IR and DBT-TU-JU and the average segmentation accuracies obtained on these databases are 72.18% and 71.26% respectively, which are better than other state-of-the-art methods. Beside this, a novel framework to analyze TBIs is proposed for differentiating abnormal and normal breasts on the basis of the segmented SRs. We have also shown experimentally that investigating only the SRs instead of the whole breast is more effective in differentiating abnormal and normal breasts.

**Index Terms**—SCH-CS, DLPE, suspicious region, thermal breast image, level set method.

## I. INTRODUCTION

Breast cancer is one of the commonest and deadliest forms of diseases in females worldwide [1]. However, it is well known that if a tumor is diagnosed in its very early stage, the mortality rate can be reduced. In this regard, different kinds of imaging modalities have been developed for the diagnosis of breast cancer in its premature stage [1]. Among those, mammography is undoubtedly considered as the most

Manuscript received xx xx, xxxx; revised xx xx, xxxx. The authors wish to thank the Ministry of Electronics and Information Technology (MeitY), Govt. of India for the grant of Visvesvaraya doctorate fellowship award to the first author. The work is partially supported by the Department of Biotechnology (DBT), Govt. of India under grant no. BT/533/NE/TBP/2014. Authors are also thankful to CMATER laboratory of the Computer Science and Engineering Department of Jadavpur University, India, for providing necessary infrastructure to carry out this research.

\*Corresponding Author: S. Pramanik.

S. Pramanik, D. Banik, D. Bhattacharjee, and M. Nasipuri are with the Computer Science and Engineering Department, Jadavpur University, India (e-mail: [srv.pramanik03327@gmail.com](mailto:srv.pramanik03327@gmail.com), [debu.cse88@gmail.com](mailto:debu.cse88@gmail.com), [debos@ieee.org](mailto:debos@ieee.org), [mitanasipuri@gmail.com](mailto:mitanasipuri@gmail.com)).

M. K. Bhowmik is with the Computer Science and Engineering Department, Tripura University, India ([mrinalkantibhowmik@tripurauniv.in](mailto:mrinalkantibhowmik@tripurauniv.in)).

Dr. G. Majumdar is with the Government Medical College (AGMC) and Regional Cancer Centre (RCC), Tripura, India ([dr.g.majumdar@yahoo.in](mailto:dr.g.majumdar@yahoo.in)).

reliable screening method. However, in spite of substantial advantages, it also has some limitations that influenced the researchers to develop new imaging modalities [1]. Nowadays, thermal imaging is extensively used as a non-invasive medical imaging modality for early prediction of the disease [1], [2]. In particular, for breast cancer detection, thermal imaging has received a tremendous amount of attention from the researchers across the world due to its intrinsic advantages over the other imaging modalities [1], [2]. The presence of a malignancy in the breast produces a higher temperature than the normal breast tissue due to a high metabolism and increased rate of blood flow to supplement the growth of a tumor. The increase in temperature in the tumor area causes an alteration in the breast skin surface temperature. Any thermal camera records this temperature distribution with a high degree of accuracy by measuring the infrared radiation emitted by the region [1], [2]. In a thermal breast image (TBI), the high-temperature regions of the breast appear as hot spots. In practice, experienced medical practitioners compared the structure of the hot spots of two breasts in order to make a diagnosis of the breast cancer. However, due to the limitation of the human vision system, medical practitioners often failed to identify such regions with an acceptable degree of accuracy and thus fail to measure asymmetry between the hottest regions of two breasts accurately. These facts have prompted researchers to develop a computer-assisted tool for the analysis of the TBIs. In effect, various methods have been developed over the past one decade [1], [3]–[6]. The majority of those methods consider the entire breast region to discern the abnormality in the breast. In [4]–[6], authors have shown that multifractal analysis is more effective in differentiating normal and abnormal breasts in breast thermograms. They have used wavelet transform modulus maxima (WTMM) [7] based multifractal analysis method for distinguishing normal and abnormal breasts. In [8], [9], a 3D computational model of the breast is prepared for the quantitative and qualitative studies of thermal breast images. Through simulation, they have analyzed the effect of tumors of varying sizes situated at varying depths below the skin on the thermal profile over the surface of the skin. By this study, they have proposed an emissivity insensitive infrared imaging technique and analyzed the captured images using frequency and time-domain methods. However, the hottest regions in a breast thermogram are the only indicator for the presence of malformation, and analysis of those regions would produce more accurate diagnosis results. Till date, very few research works have analyzed breast thermograms based on hottest region segmentation [10], [12], and this might be due

to the various challenges associated with the segmentation of the hottest regions from the breast thermograms. The primary challenge is the complex background of TBI making the hottest region segmentation quite complicated. Secondly, the non-uniform intensity distribution, poor contrast, incomplete object boundaries, blurriness, and noise are some of the major issues that need to be handled properly to segment the hottest regions. Typically, the non-uniform intensity in the image causes regions to overlap each other which makes the segmentation task more difficult. Moreover, the variability and complexity of the hottest regions increase the difficulty of segmenting hottest regions.

The existing hottest region segmentation methods comprise clustering-based methods [11], [14], color quantization-based method [12], active contour-based method (ACM) [13], and Hybrid intelligence technique [1]. Table-I summarizes the state-of-the-art hottest region segmentation methods. However, among the existing methods, the ACM, named as CV-LSM [13], performs comparatively better for the segmentation of the hottest region, and this fact has motivated us to use the ACM-based method for the segmentation of the suspicious regions (SRs)<sup>1</sup> in breast thermograms. Over the last few decades, level set (LS), an implicit ACM, has been widely used for the segmentation of medical images [15]–[19]. According to the level set theory, the contours are implicitly represented by zero level set function, and it is considered as one of the parameters for the minimization of the energy functional [20]. The zero level set is basically defined in the image domain and using the pixel information as a force (internal and external) it is driven towards its desired location. Based on the image features used in the energy functional, existing level set methods can be grouped into the following two types: edge-based methods (EMs) [16], [17] and region-based methods (RMs) [15], [18], [19]. However, the EMs often suffer from over, under-segmentation, and boundary leakage as in most of the medical images the presence of edges is vague. On the other hand, the RMs can perform well in the presence of blurred object boundaries and noise. However, both the LSMs are very much sensitive to the initial contour location. Typically, an inappropriate initialization of the level set function (LSF) may increase the number of iterations which in effect, increase the overall execution time. Also, the time consuming re-initialization step of the level set function limits their use in SRs segmentation.

In this work, we have proposed a novel, fast, region-based active contour model for the precise segmentation of the suspicious regions, which is the primary contribution of this work. The proposed segmentation method can effectively handle the problems associated with the segmentation of the SRs without any human intervention. Firstly, a novel, adaptive thresholding method SCH-CS is proposed to segment the highly homogeneous regions inside the potential SRs, which are later used to initialize the zero LSF accurately. Then, to handle non-uniform intensity distribution near the boundaries of SRs, we define a new energy functional, called DLPE.

<sup>1</sup>Note: In this work, we call the hottest regions corresponding to the breast region as the suspicious regions (SRs).

The proposed DLPE is then transformed into a corresponding level set formulation and minimized using the interleaved operation of the level set evolution to segment the SRs accurately. Additionally, a distance regularized penalty term (DRPT) is added to the proposed energy functional to avoid time-consuming re-initialization steps. Moreover, to stop the evolution of the proposed active contour model numerically, a new stopping criterion is proposed based on LSF. Finally, we have proposed a novel system, called suspicious-regions-based thermal breast image analysis (STBIA), to effectively differentiate the normal and abnormal breasts. The segmentation results are qualitatively and quantitatively validated using the ground truths and also compared with those of three state-of-the-art SR segmentation methods on the same ground truths. Some notable contributions of this paper can be outlined as follows.

- *Identification of SRs using the proposed SCH-CS method:* By incorporating the results of SCH-CS as the initial evolving curves of the LSM, we ameliorate not only the efficiency of the LSM, but also the accuracy of the segmentation results.
- *DLPE Energy Functional based Level Set Formulation:* This formulation gives different priorities to the pixels in the neighborhood to handle nonuniform intensity distribution near the boundaries of SRs, and in effect accurately segments the SRs.
- *Development of a New Stopping Criterion and Adaptive Estimation a Controlling Parameter of the LSM:* This makes the segmentation method fully automatic and more efficient.
- *Design of a Novel System Based on the Segmented SRs for the Differentiation of the Abnormal and Normal Breasts:* The proposed system significantly improves the differentiation accuracy compared to the systems which focus on the whole breast thermograms.
- *Development of Two Sets of Ground-Truths:* Two sets of ground-truths are developed and used to avoid the single expert's biasness and accurately evaluated the segmentation results.

The rest of this paper is systematized as follows. Section-2 presents the proposed SR segmentation method. In section-3, a SR based thermal breast image analysis system is described. Detailed experimental setup and results are discussed in Section-4. Concluding remarks are presented in section-5.

## II. SUSPICIOUS REGION SEGMENTATION

In this section, we describe our proposed fully automatic SR segmentation method which is based on sequential applications of three techniques: an adaptive thresholding method (SCH-CS), a function embedding different priorities locally, called different local priorities embedded (DLPE) energy function, and a level set method (LSM). Fig. 1 illustrates the flow diagram of the proposed segmentation method. Let us assume that  $p : \Xi \rightarrow \mathbb{R}^+$  be a gray-level TBI, where  $\Xi \subset \mathbb{R}^2$  signifies the image domain. The regions in an abnormal TBI can typically be classified into three kinds, such as the background region (BR), normal tissue region, called tissue background region (TBR), and SRs.

Table I  
SUMMARY OF STATE-OF-THE-ART HOTTEST REGIONS SEGMENTATION METHODS.

Ref.	Methodology	Database Used/ Image Type	No. of images used	Limitations
[11], [14]	Clustering techniques: k-means, Fuzzy c-means (FCM), and mean shift (MS)	Private database/ Color	6,60	FCM performs better than k-means and MS methods. Use of pseudo color image may produce inconsistent segmentation results. Because of the temperature vs. color mapping method may differ from device to device. No method is used to identify the potential hottest regions.
[12]	Minimum variance quantization (MVQ) method	Private database/ Color	40	The system is not described clearly and also, the use of the pseudo color image may bring a similar problem as in [11], [14].
[13]	Active contour-based method: Chan-Vese level set method (CV-LSM)	Private database/ Color	30	CV-LSM works better than the k-means, FCM, and MS methods. The initial contour location of CV-LSM is not specified. The use of the pseudo color image may produce a similar problem as in [11], [12], [14].
[1]	Hybrid intelligence technique: a sequential hybrid intelligence technique	Public: DMR-IR database/ Color	40	This method overcomes the problem of the potential hottest color region identification as in [11], [12], [14]. The use of pseudo color image may bring similar problem as in [11], [12], [14].



Figure 1. Flow diagram of the proposed segmentation method.

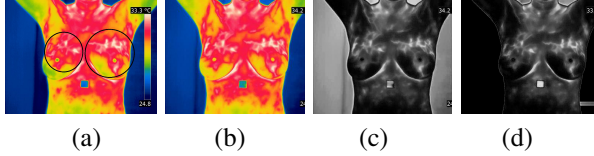


Figure 2. (a) original pseudo-color TBI with confirmed hottest regions marked with black circles, (b) image without color-scale (c) grayscale image, and (d) background removed image.

### A. Pre-processing

Usually, in a pseudo-color TBI, a color scale of fixed width appears alongside the image at a fixed position, as shown in Fig. 2(a). Thus, the color scale is first automatically removed from the TBI, using the width and positional information of it, as shown in Fig. 2(b). Each pixel value in the pseudo-color TBI represents the body temperature as a 24-bit (three-byte) number. Hence, from this cropped image, only the most significant byte of each pixel value is extracted to form a grayscale image of breast thermogram [Fig. 2(c)]. Thus this grayscale image contains the information about the hottest regions, and is useful in the present work. It has been experimentally seen that the most significant byte image also provides the maximum contrast between the SRs and other regions in TBI. In the preprocessing step, BR is removed from the gray-scale image using Otsu's thresholding, and then a gray-level reconstruction method as proposed in [21] is applied on it. The resulting image is shown in Fig. 2(d).

### B. Identification of suspicious regions

A meticulous study of the TBIs, performed in this work, reveals some facts about the SRs and TBR. Firstly, the SR is a connected and cohesive region which has an average intensity above that of the rest of the image. The intensities

in the central area of a SR are highly homogeneous while this homogeneity gradually decreases towards the boundaries. Again, most importantly, the size of a SR is relatively small in comparison to the whole breast. On the other hand, the intensities in the TBR are non-uniformly distributed with a high degree of inhomogeneity. By considering the above facts, we have proposed a novel technique based on the selection of smaller-peaks corresponding to the high-intensity-pixels (SCH) and the centroid-knowledge of SRs (CS), named SCH-CS, to approximately segment the SRs from the TBI. Firstly, an adaptive thresholding method is proposed based on SCH to locate the approximate SRs from the TBI. Then, CS is used to isolate the actual SRs.

Gray level histogram analysis is the most popular technique in automatic gray-level thresholding if the region of interest is identifiable from the background region. However, by observing the histograms of the background removed grayscale TBIs, it is noted that the histograms are multimodal, valleys are relatively wide and shallow, and the peaks vary significantly in size, see Fig. 3(b). Thus, in this work, instead of looking for valleys, we use information about peaks in the histogram for the selection of the desired threshold. Let  $p_b$  be the background removed grayscale TBI, and  $H$  be the gray level histogram of the image  $p_b$  defined over a set of gray levels  $S$ , where  $S = (n_0, n_1, \dots, n_{L-1})$  and  $L$  signifies the number of gray levels. Let the frequency of occurrences of these gray levels in  $p_b$  be represented as  $h(n_0), h(n_1), \dots, h(n_{L-1})$ . The desired threshold  $th$  for the segmentation of the SRs from the  $p_b$  is calculated from the histogram  $H$ . Any peak in the histogram contributes significant information for the selection of a threshold, but not equally during the selection of a threshold from the histogram. Also, the selection of peaks entirely depends on the given problem. Therefore, in this work, we select those peaks whose values are less than a value named

as count threshold (CT), denoted by  $\rho$ . As mentioned earlier, the SR in a thermal breast image is relatively a smaller region concerning the entire breast, which means the histogram bins corresponding to the gray-levels in the SR, will have smaller peaks. This property of the SR motivated us to use histogram peaks instead of valley information. The count threshold  $\rho$  is calculated as follows:

$$\rho = \frac{\max[h(n_0), h(n_1), \dots, h(n_{L-1})]}{C} - m \quad (1)$$

where,  $C = N/V$ ,  $V = \sum_{i=0}^{L-1} h(n_i)/r$  where  $h(n_i) > m$ ,  $m = 1/R \sum_{i=0}^{L-1} h(n_i)$ ,  $N = \sum_{i=0}^{L-1} h(n_i)$ ,  $r$  is the number of peaks which have value greater than  $m$ , and  $R$  is the number of available gray levels in the specified image.

Let  $A = [n_1, n_2, \dots, n_j]$  be an array of gray-levels of the peaks selected using CT  $\rho$ . Thus, the mean  $m^{(A)}$  and standard deviation  $\alpha^{(A)}$  of  $A$  are computed to estimate an initial threshold  $t^*$ . The  $t^*$  is computed as follows:

$$t^* = m^{(A)} - \alpha^{(A)} \quad (2)$$

Now, the threshold  $th$  is computed as follows:

$$th = \begin{cases} m^{(p)}, & \text{if } t^* < m^{(p)} \\ t^*, & \text{Otherwise} \end{cases} \quad (3)$$

where,  $m^{(p)} = 1/uv \sum_{i=1}^u \sum_{j=1}^v p_b(i, j)$  is the mean gray-level of the image  $p_b$ . After calculation of a threshold  $th$ , a pixel in  $p_b$  is classified as either a TBR pixel or a SR pixel using the following rule. If  $p_b(i, j) \geq th$ , then  $p_b(i, j)$  is considered as a pixel of SR; otherwise, it considered as the TBR pixel.

After applying the threshold  $th$ , the resultant image includes not only the SRs but also other high-intensity regions present in the  $p_b$ , shown in Fig. 3(c). Typically, the inframammary fold regions, armpit regions, and lower neck regions in a TBI are also the high-intensity regions. Therefore, the thresholded image includes all such regions along with SRs, which are shown in Fig. 3(c), where SRs are marked with green circles. Thus, it is necessary to isolate only SRs to process it further. By observing Fig. 3(c), it is noted that the SRs are typically spread over a horizontal region near the middle part of the image, and they are connected and have definite centroid. Therefore, in this paper, the centroid-knowledge of SRs (CS) is used to isolate the actual SRs of breast thermogram.

The detailed algorithm (CS) for isolation of the SRs is as follows. Let us assume that  $p_b^{th}$  be the thresholded binary image. In the first step, the centroid  $R_c^{(k)}$ , for each region  $k$  in  $p_b^{th}$ , is calculated using eq. (4) [23]. Then, the average centroid  $C_{avg}^{(1)}$  is calculated. Now, the regions are eliminated using the following rule. If  $R_c^{(k)}(X) < C_{avg}^{(1)}(X)$ , then the  $k^{th}$  region  $R_c^{(k)}$  is eliminated. In the next step, the average centroid  $C_{avg}^{(2)}$  of the remaining regions are calculated, and the regions having  $R_c^{(k)}(X) > C_{avg}^{(2)}(X)$  are eliminated. Again, calculate the average centroid  $C_{avg}^{(q)}$  of the regions obtained from the previous step and if  $|R_c^{(k)}(X) - C_{avg}^{(q)}(X)| \leq \varepsilon$ , then stop the iterations. Otherwise, repeat the steps. After several experimentations, the optimal performance for isolation of SRs is obtained with the value of  $\varepsilon$  as 35.

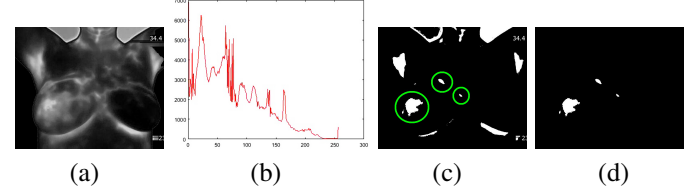


Figure 3. (a) grayscale image after background removal, (b) corresponding histogram, (c) SRs marked with green circles along with other hottest regions, (d) final approximated SRs by SCH-CS.

$$R_c^{(k)} = (X, Y); X = \frac{\sum R^{(k)}(i, j) * i}{\sum R^{(k)}(i, j)}; Y = \frac{\sum R^{(k)}(i, j) * j}{\sum R^{(k)}(i, j)} \quad (4)$$

where,  $R_c^{(k)}$  is the  $k^{th}$  region centroid,  $R^{(k)}(i, j)$  is the  $k^{th}$  region intensity value at coordinate  $(i, j)$ . It is noted that sometimes the centroid may lie outside the boundary of the approximated suspicious region, because of the concave shape of the region. To overcome this issue we have proposed a method based on a bounding box, which is summarized in Algorithm-1, to always restrict the centroid inside the boundary of the suspicious region.

---

#### Algorithm 1 Restrict the centroids inside the SRs

---

- 1: Input:  $p_b^{th}$  with SRs having centroids outside the actual boundaries of the SRs.
  - 2: Output:  $p_b^{th}$  with SRs having centroids inside the regions
  - 3: for  $k = 1$  to  $n$  do
  - 4: if  $R_c^{(k)}(i, j)$  is outside of the SR  $R^{(k)}$
  - 5: Calculate the Bounding Box  $BB^{(k)}$  for  $R^{(k)}$ . Let  $\{BB_q^{(k)} | 1 \leq q \leq 4\}$  represents 4 corner points of  $BB^{(k)}$
  - 6: for each point  $q = 1$  to  $4$  in  $BB^{(k)}$  do
  - 7:  $D_q(i, j) = \frac{\|R_c^{(k)}(i, j) - BB_q^{(k)}\|}{2}$
  - 8: end for
  - 9: Compute new centroid  $R_c^{(k)}(i, j) = \min[D_q(i, j)]$
  - 10: end if
  - 11: end for
- 

It is noted that the thresholding technique, proposed above, is not sufficient to segment the SRs accurately from the TBI. Very often it segments subsets of SRs which have global superiority in terms of high intensities over the image. In other words, it segments the highest intensity regions of the SRs, which are highly homogeneous. Hence, these results are used to initialize the proposed level set method appropriately, discussed in the following section.

#### C. Segmentation of overlapped suspicious regions

Nonuniform intensity distribution (NID) causes regions overlap in a TBI, which is a big problem like other imaging modalities for the segmentation of the region of interest. In order to better understand the effect of NID, we have considered the following most popularly used multiplicative NID model [24]:

$$p(i, j) = \mathfrak{B}(i, j)\bar{p}(i, j) + \mathfrak{n}(i, j) \quad (5)$$

where  $p : \Xi \rightarrow \Re^+$  denotes the given input image,  $\mathfrak{B} : \Xi \rightarrow \Re^+$  is the non-uniform intensity field (NIF) which is assumed to be smooth in  $\Xi$ ,  $\bar{p} : \Xi \rightarrow \Re^+$  is the true image signal which is considered as piecewise constant in the domain of each region, and  $n : \Xi \rightarrow \Re^+$  signifies the additive Gaussian noise. Here, the objective is to estimate  $\bar{p}$  so that the regions in  $\bar{p}$  should have sharp discontinuities to get better segmentation results. Neglecting noise, the eq. (5) is rewritten as follows:

$$p(i, j) = \mathfrak{B}(i, j)\bar{p}(i, j) \Rightarrow \bar{p}(i, j) = \frac{p(i, j)}{\mathfrak{B}(i, j)} \quad (6)$$

Now the question is how to estimate  $\mathfrak{B}$ ? In practice, typically, the NIF  $\mathfrak{B}$  is approximated by applying a low-pass filter on the original image  $p$ , divided by a normalized constant  $N_c$ . In a recent paper [25], the authors have used spatial average-filter as a low-pass filter to estimate  $\mathfrak{B}$ . However, the common problem with the average-filter is that it gives the equal priority to all the pixels in the specified window. As remarked earlier,  $\mathfrak{B}$  is a low-frequency component which does not contain any sharp change in pixel intensity values. Thus in  $\mathfrak{B}$ , the high-intensity pixels suffer more than the low-intensity pixels [26]. In a TBI, high-intensity pixels constitute the suspicious region. Thus, it is necessary to give higher weightage to the high-intensity pixels than the low-intensity pixels for the estimation of the  $\mathfrak{B}$  in a TBI. In this regard, Contraharmonic Mean (CHM) filter has been successfully used in [26] to estimate  $\mathfrak{B}$  since it non-linearly updates the intensities in the image.

*Proposition 2.1:* The CHM-filter of order  $n > 0$  has more potentiality to estimate the NIF  $\mathfrak{B}$  compared to the spatial average-filter.

The detailed theoretical justification of *Proposition 2.1* can be found in [26]. In this work, we have thus used CHM-filter to estimate the  $\mathfrak{B}$  and in effect to obtain approximately piecewise constant intensity image  $\bar{p}$ . Thus,  $\mathfrak{B}$  is computed as follows:

$$\mathfrak{B}(i_c, j_c) = CHM_{W(i_c, j_c)} / N_c \quad (7)$$

where  $CHM_{W(i_c, j_c)}$  is a CHM filter with order  $n = 1$ , defined in (8).  $W$  is a local window of size  $9 \times 9$  centered at coordinate  $(i_c, j_c)$ ,  $N_c$  is a normalizing constant defined in (9).

$$CHM_{W(i_c, j_c)} = \frac{\sum_{(i,j) \in W(i_c, j_c)} p^{n+1}(i, j)}{\sum_{(i,j) \in W(i_c, j_c)} p^n(i, j)} \quad (8)$$

$$N_c = \frac{\sum_{(i,j) \in \Xi} p^{n+1}(i, j)}{\sum_{(i,j) \in \Xi} p^n(i, j)} \quad (9)$$

Putting (7) into (6) we have

$$\bar{p}(i, j) = \frac{p(i, j)N_c}{CHM_{W(i_c, j_c)}} \quad (10)$$

After that, to appropriately segment the suspicious regions, we have proposed a new energy functional based on (10), called different local priorities embedded (DLPE) energy functional. The DLPE energy functional can be defined as follows:

$$F_{DLPE}(l_1, l_2, C) = \alpha_1 \int_{in(C)} \left| \frac{p(i, j)N_c}{CHM_{W(i_c, j_c)}} - l_1 \right|^2 didj + \alpha_2 \int_{out(C)} \left| \frac{p(i, j)N_c}{CHM_{W(i_c, j_c)}} - l_2 \right|^2 didj \quad (11)$$

where  $C : \Re \rightarrow \Xi$  signifies the closed contour,  $in(C)$  and  $out(C)$  define the inside and outside regions of  $C$ , and  $l_1$  and  $l_2$  are the intensity means of  $\bar{p}$  computed over inside and outside regions of  $C$  as follows:

$$l_1 = \frac{\int_{in(C)} \bar{p}(i, j) didj}{\int_{in(C)} didj}; l_2 = \frac{\int_{out(C)} \bar{p}(i, j) didj}{\int_{out(C)} didj} \quad (12)$$

To effectively handle the topological changes, the contour  $C$  in (11) is formulated using the level set function (LSF). Typically, the LSF  $\phi$  is an implicit representation of the closed contour  $C$ . By definition, a closed contour  $C \subset \Xi$  can be replaced by the zero level set of a Lipschitz function  $\phi : \Xi \rightarrow \Re$  [27]. Now, the proposed energy functional (11) is expressed regarding zero LSF  $\phi$  as follows:

$$F_{DLPE}(l_1, l_2, \phi) = \alpha_1 \int_{\Xi} \left| \frac{p(i, j)N_c}{CHM_{W(i_c, j_c)}} - l_1 \right|^2 H_{\varepsilon}(\phi(i, j)) didj + \alpha_2 \int_{\Xi} \left| \frac{p(i, j)N_c}{CHM_{W(i_c, j_c)}} - l_2 \right|^2 (1 - H_{\varepsilon}(\phi(i, j))) didj \quad (13)$$

where,  $H_{\varepsilon}(\phi(i, j))$  is the smooth approximation of the Heaviside function  $H(\phi(i, j))$  [15].

The energy functional defined in (13) includes only the data fitting term which is not sufficient for the smooth evolution of the LSF. During the evolution of the zero LSF by minimizing (13), small or isolated contours can develop in the final segmented image. Therefore, in this work, we have used a length penalty term (LPT) in (13), as used in [15], to smooth the evolving contour so that problems stated above can be avoided. Another fundamental problem of traditional LSM is the time-consuming re-initialization step, which is generally used to prevent irregularities caused during the evolution of the LSM. Thus, a distance regularized potential term (DRPT) [16] is included in (13) to avoid such time-consuming re-initialization step. The LPT  $\mathbb{L}(\phi = 0)$  and DRPT  $\mathcal{D}_p(\phi)$  of the zero level set  $\phi$  are defined as follows:

$$\mathbb{L}(\phi = 0) = \int_{\Xi} |\nabla H_{\varepsilon}(\phi(i, j))| didj = \int_{\Xi} \delta_{\varepsilon}(\phi(i, j)) |\nabla \phi(i, j)| didj \quad (14)$$

$$\mathcal{D}_p(\phi) = \int_{\Xi} \frac{1}{2} (|\nabla \phi(i, j)| - 1)^2 didj \quad (15)$$

where,  $\delta_{\varepsilon}$  is the smooth approximation of the Dirac delta function  $\delta$ , which is computed by taking the derivative of  $H_{\varepsilon}(\phi(i, j))$  [15], respectively.

*Proposition 2.2:* DRPT eliminates the re-initialization procedure by penalizing the deviation of  $\phi$  from the sign distance function (SDF).

Irregularities of the LSF make the computation of the numerical approximation highly inaccurate, which further deteriorates the stability of the evolution of the LSF [16]. Therefore, to prevent such problem, the LSF  $\phi$  is transformed to the SDF at the beginning of the evolution of  $\phi$ . Then, this sign distance property is maintained throughout the evolution by periodically re-initializing it in a SDF. The re-initialization can be done by solving the eikonal equation:  $|\nabla \phi| = 1$ , with  $\phi = 0$  on  $\phi(t=0) = 0$ , which is a very time-consuming task. In contrast, DRPT in (15) maintains the regularity in shape of the

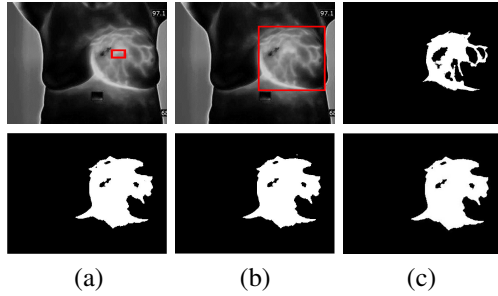


Figure 4. Segmentation results for (a-b) manually initialized square inside the SR (877 iterations, ET: 22.46s) and outside the SR (476 iterations, ET: 18.47s), and (c) our initialization scheme (300 iterations, ET: 8.95s).

LSF by driving its gradient magnitude to one of its minima points, specifically a sign distance property close to its zero LSF. The detailed theoretical justification of *Proposition-2.2* can be found in [16].

Thus the proposed energy functional is finally formulated using (13), (14), and (15) as follows:

$$E_{DLPE}(\phi, l_1, l_2) = F_{DLPE}(l_1, l_2, \phi) + \vartheta \mathbb{L}(\phi = 0) + \theta \mathcal{D}_p(\phi) \quad (16)$$

The fundamental dissimilarity between the proposed  $E_{DLPE}$  and the method mentioned in [25] is the use of CHM filter in  $E_{DLPE}$  (spatial average filter is used in [25]). This may be considered as a novelty of our proposed method. In effect, the energy functional in [25] classifies the boundary pixel of a SR as the TBR pixel and shrinks the actual size of the SR. The proposed LSM works in two stages as described below:

1) *Initialization of the level set function:* Automatic and accurate initialization of the level set function is a most desirable criterion for the steady evolution of the contour. The majority of the related papers [15], [18], [19] have used manual initialization, and also they claimed that their methods are insensitive to the initialization. However, their claim is justifiable only when the background region in the image has approximately similar intensities. As mentioned in section-I, the complex background in a TBI is one of the primary challenges for the segmentation of the SRs. Therefore, it is indispensable to define proper initialization of the level set function. In this work, we have used the segmentation results of SCH-CS discussed in section-II(B) for the initialization of the level set function. Let  $p_b^{th}$  be the binary image containing approximated SRs obtained by applying SCH-CS, where intensity 1 corresponds to the SRs and 0 corresponds to the BR or TBR. The initialization of the level set function  $\phi$  at time  $t = 0$  can be defined as follows:

$$\phi_{t=0}(i, j) = 4 * p_b^{th} - (1 - p_b^{th}) * 4 \quad (17)$$

Fig. 4 illustrates the segmentation results of different initializations. As shown, the proposed initialization scheme segmented the SR with less number of iterations and execution time (ET). Therefore, it is safe to conclude that the proper initialization is extremely important in the level set method to automate the level set evolution and ameliorate its efficiency.

2) *Energy minimization and numerical implementation:* In the present work, we have used traditional gradient descent technique to minimize the proposed energy functional (16).

For fixed  $l_1$  and  $l_2$ , the minimization of  $E_{DLPE}(\phi, l_1, l_2)$  concerning  $\phi$  can be accomplished by solving the gradient descent flow equation with the initial level set condition and Neumann boundary conditions as

$$\begin{aligned} \frac{d\phi}{dt} = \delta_\varepsilon(\phi) &[-\alpha_1(\frac{p(i, j)N_c}{CHM_{W(i_c, j_c)}} - l_1)^2 + \alpha_2(\frac{p(i, j)N_c}{CHM_{W(i_c, j_c)}} - l_2)^2] \\ &+ \vartheta \delta_\varepsilon(\phi) \operatorname{div}(\frac{\nabla\phi}{|\nabla\phi|}) + \theta(\nabla^2\phi - \operatorname{div}(\frac{\nabla\phi}{|\nabla\phi|})) \end{aligned} \quad (18)$$

$\phi(0, i, j) = \phi_0(i, j) = 4 * p_b^{th} - (1 - p_b^{th}) * 4$  in  $\Xi$ ;  $\frac{d\phi}{dn} = 0$  on  $d\Xi$ ; where,  $t \geq 0$  is a time variable and  $d\Xi$  is the boundary.

Similarly, by keeping  $\phi$  fixed,  $E_{DLPE}(\phi, l_1, l_2)$  can be minimized with respect to  $l_1$  and  $l_2$ . Using the calculus of variation, the optimal  $l_1$  and  $l_2$  that minimizes  $E_{DLPE}(\phi, l_1, l_2)$  are defined as follows:

$$l_1 = \frac{\int_{\Xi} \bar{p}(i, j) H_\varepsilon(\phi(i, j)) didj}{\int_{\Xi} H_\varepsilon(\phi(i, j)) didj} \quad (19)$$

$$l_2 = \frac{\int_{\Xi} \bar{p}(i, j)(1 - H_\varepsilon(\phi(i, j))) didj}{\int_{\Xi} (1 - H_\varepsilon(\phi(i, j))) didj} \quad (20)$$

The finite difference techniques in the numerical method are commonly used to discretize and approximate the partial differential equation in (18). The finite difference techniques, as used in [15], are also adopted in this work to implement the proposed energy functional (18) numerically.

As can be seen from eq. (16),  $E_{DLPE}$  value keeps decreasing when the active contour evolves toward the actual region boundaries and finally, iteration will stop while  $E_{DLPE} \approx 0$ , which is difficult to be implemented using finite difference techniques. It is tough to find any work that has used stopping criterion of numerically efficient. In this work, we have proposed a new form of stopping criterion to stop the level set function at the true region boundaries numerically. During the level set evolution, we observed that when the level set function reaches the precise region boundaries, the value of  $\phi$  does not change anymore. Based on this observation, the proposed stopping criterion is defined as follows:

$$|1 - r(\phi^{N-1}, \phi^N)| \leq t_{stop} \geq |1 - r(\phi^N, \phi^{N+1})| \quad (21)$$

where,  $N > 5$ ,  $\phi^N$  signify the level set function at  $N^{th}$  iteration, and  $r$  indicates the correlation coefficient. After several experiments, we have chosen the value of stopping threshold  $t_{stop}$  as 0.05.

### III. SUSPICIOUS-REGION-BASED TBI ANALYSIS SYSTEM

In this section, we demonstrate our proposed suspicious-region-based thermal breast image analysis (STBIA) system. Fig. 5 shows the flow diagram of the STBIA system.

#### A. Feature Extraction and Classifier Design

After segmentation of the SRs, a set of texture and structural features is extracted from them to differentiate between normal and abnormal breasts. In this work, Haralick features and Hu's moment invariants are used as the texture and structural features.

Haralick features are the second order statistical features extracted from the gray-level co-occurrence matrix (GLCM) of an image [28], which are most popularly used features in

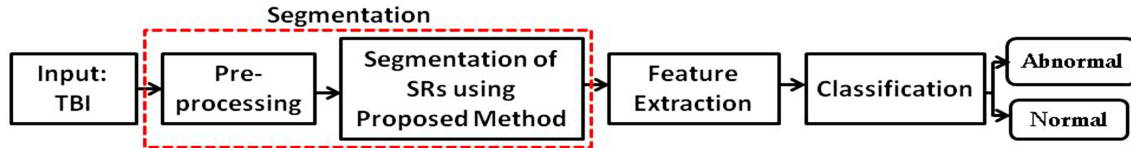


Figure 5. Flow diagram of the proposed STBIA system.

the domain of thermal breast image analysis. In the present work, firstly, we have calculated the GLCM  $G(u, v/1, \theta^\circ)$  of  $p_b^s$  (obtained in section-II). Then, its transpose is added to it in order to make symmetric. After that, the normalized GLCM is obtained by (22)

$$g_{p_b^s}(u, v) = \frac{G^{sym}(u, v/1, 0^\circ)}{\sum_{u=1}^L \sum_{v=1}^L G^{sym}(u, v/1, 0^\circ)} \quad (22)$$

where  $G^{sym}(u, v/1, 0^\circ) = G(u, v/1, 0^\circ) + G^T(u, v/1, 0^\circ)$ ,  $G^T$  signify the transpose of  $G$ , and  $L$  is the number of gray levels in  $p_b^s$ . Finally, fourteen Haralick features [28] are extracted from  $g_{p_b^s}$ .

In 1962, Hu first introduced moment invariants [29], based on the concept of geometric moments, Hu derived total seven moment invariants. The most attractive properties of the Hu's moment invariants that make them robust and acceptable measures for tracing image patterns are their invariance to translation, rotation, and scaling. These properties have motivated us to use it in the analysis of the thermal breast images which are often affected by the translation and scaling. To the best of our knowledge, Hu's moment invariants have never been studied for the analysis of the thermal breast image.

After computation of Haralick features and Hu's moment invariants, they are concatenated to form 21-elements feature vector for each breast. Let  $[f_v^{(L)}]_{1 \times 21}$  and  $[f_v^{(R)}]_{1 \times 21}$  are demonstrating the feature vectors of the left and right breasts respectively of each patient. Then, the asymmetry feature vector  $[F]_{1 \times 21}$  is calculated for each patient breast thermogram by taking the absolute difference between corresponding elements of  $f_v^{(L)}$  and  $f_v^{(R)}$ , i.e.,  $F = |f_v^{(L)} - f_v^{(R)}|$ .

In this work, a three-layer feed-forward artificial neural network (FANN) [23] is used for the classification purpose. In the input layer of the network contains twenty-one neurons to fit the twenty-one elements feature vector,  $F$ . Selection of the appropriate number of neurons in the hidden layer is itself a non-trivial problem. In this work, we experimentally choose forty-two neurons in the hidden layer. Since our problem of classification is a two-class partitioning problem, the output layer of the network thus includes only one neuron. The Linear transfer function is used for all the neurons in the input layer. Similarly, the hyperbolic tangent transfer function and softmax transfer function are used for all the neurons present in the hidden and output layers respectively. The Levenberg-Marquardt back-propagation algorithm (with learning rate=0.1) is used to train the network.

#### IV. EXPERIMENTAL RESULTS AND DISCUSSION

In this section, we present the detail of the experimental results of our proposed system. In the subsection-A of this section, the database of breast thermograms used in this work

is described. In the subsection-B, the quality of the segmentation results obtained by the proposed method is evaluated concerning the ground-truths generated by the experts. In subsection-C, the efficacy of the proposed STBIA system in the diagnostic analysis of TBI is studied.

As seen in eq. (18), some parameters such as  $\alpha_1, \alpha_2, \vartheta$ , and  $\theta$  are associated with the proposed energy functional, which are called controlling parameters. In this work, the following parameter values are experimentally defined:  $\alpha_1 = \alpha_2 = 1$ , and  $\theta = 0.2$ . The length controlling parameter  $\vartheta$  is adaptively set based on the SCH-CS segmentation results. The value of  $\vartheta$  is defined as  $\vartheta = (0.1 * 255)/k$ , where  $k$  is the number of SRs produced by SCH-CS. As stated in subsection-II(B), the sizes of the SRs are relatively small and vary from image to image. Moreover, even for the same image, the SRs vary in size. If an image consists of several SRs, the value of  $\vartheta$  will be small. In effect, the proposed level set method will identify all the potential SRs of any size.

##### A. Database of breast thermograms

The breast thermograms used in this research work are collected from the existing DMR-IR (Database for Mastology Research with Infrared Image) [30] and DBT-TU-JU (Department of Biotechnology-Tripura University-Jadavpur University)[33] databases. DMR-IR is an open-access online database that consists of breast thermograms of total 287 patients of which 240 cases are normal whereas 47 are confirmed as abnormal cases. Besides, DBT-TU-JU database consists of a total 100 patients breast thermograms of which 51 cases are reported as normal whereas 49 cases are abnormal. From the DMR-IR and DBT-TU-JU databases, 65 (35 normal and 30 abnormal) and 90 (46 normal and 44 abnormal), respectively, frontal view breast thermograms with confirmed hot spots in one or both breasts are randomly selected for our work. It is noted that, in this work, we have used total 155 frontal view breast thermograms for our experiment purpose, which is considerably larger than those used in the past works (see Table-I).

##### B. Experiment 1: Qualitative and Quantitative evaluation of the segmentation results

In this work, we have used supervised evaluation technique to evaluate the segmentation results of the proposed method. In this technique, segmentation results are typically compared with the ground-truth segmentation results using some evaluation metrics. The DBT-TU-JU database is already annotated with the ground-truth segmentation results. Besides, the DMR-IR database does not consist any ground-truths for SRs of breast thermograms. Hence, in this work, we have developed

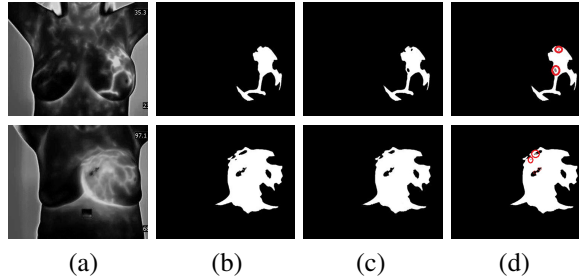


Figure 6. (a) grayscales images, (b-c) ground-truth generated by first and second experts, (d) inter-expert variation marked with red circles.

ground-truths prior to evaluating the segmentation results of the proposed method for the images of DMR-IR database used in this work. However, generation of consistent and accurate ground-truths is not an easy task, specifically, where the shape of the region-of-interest varies irregularly. Due to the unavailability of robust automatic ground-truth generation technique, researchers in the relevant fields prefer to use manual generation of the ground-truth segmentation results by the experts. However, ground-truths prepared by a single expert are not sufficient, it may be biased. In this work, we have used two experts for the generation of two different ground-truths for one TBI. It should be noted that the minimum inter-expert variation is always desirable to accurately evaluate the segmentation results. In Fig. 6, we illustrate some examples of ground-truths prepared by two experts for the images of DMR-IR database and their variations. The first column in Fig. 6, shows the grayscale TBIs. The second and third columns show the ground-truths generated by two different experts, while column four shows the union of ground-truths, respectively. The red circles in the images of Fig. 6 (d) mark the inter-expert disagreement, which is very small. Also, to show the agreement between two experts delineation of the SRs in the TBI, we have constructed Bland-Altman plot and linear regression plot, as shown in Fig. 7(a) and 8(a). It can be observed that there is a high degree of agreement between two experts delineation of the SRs. There are very few SRs outside the dotted lines (i.e., 95% confidence interval). Also, there is a very high correlation,  $R^2 = 0.997$ , between the experts (Fig. 8(a)). Thus, from the above quantitative and qualitative analysis of the ground-truth segmentation results generated by two experts, it is safe to conclude that our ground-truths are consistent. Therefore, the final ground-truth image for each breast thermogram is obtained by taking the intersection of two experts ground-truths. If  $gt_1$  and  $gt_2$  are two binary ground-truths of a breast thermogram prepared by two experts, then the final ground-truth  $gt$  is computed as  $gt = gt_1 \cap gt_2$ .

Figs. 7(b-c) and 8(b-c) illustrate the Bland-Altman and linear regression plots for the proposed method's (PM) segmentation results and the ground-truth segmentation results for the two databases. These plots are constructed to evaluate the degree of similarity between the segmentation results of the proposed method (PM) and the expert's ground-truths. The dashed lines in both the Figs. 7(b) and (c) demonstrate the agreement limit, which is also called 95% confidence interval. It can be observed that there is a high agreement between the segmentation results

Table II  
SEGMENTATION ACCURACY COMPARISON FOR BOTH THE DATABASES.

Databases		PM (%)	CV-LSM(%)	k-means(%)	FCM(%)
DMR-IR Database	Avg.	<b>72.18</b>	66.07	57.72	57.81
	Max.	<b>95.90</b>	95.47	87.62	84.03
	Min.	<b>59.20</b>	13.92	21.31	21.46
DBT-TU-JU Database	Avg.	<b>71.26</b>	63.76	52.62	52.47
	Max.	<b>91.83</b>	91.95	90.06	90.23
	Min.	<b>58.82</b>	35.91	10.21	11.11

of the proposed method and the ground-truths for both the databases. Also, Figs. 8(b) and (c) also show that there is a high correlation ( $R^2$ ) between the segmentation results obtained by PM and the ground-truths for both the DMR-IR and DBT-TU-JU databases, which are 0.9357 and 0.9232 respectively.

Further, we have computed the segmentation accuracy ( $\mathcal{A}$ ) to evaluate the segmentation results obtained by the PM against the ground-truths. Let  $p_b^s$  be the segmentation results obtained by PM, and  $gt$  be the ground-truth segmentation result. It is important to note that all the resultant images and ground-truths are binary images, where pixel value one correspond to the suspicious regions. Now, the segmentation accuracy ( $\mathcal{A}$ ) can be calculated as follows:

$$\mathcal{A} = \frac{\text{No. of correctly seg. pixels}}{\text{Total no. of pixels}} = \frac{p_b^s \cap gt}{p_b^s \cup gt} \quad (23)$$

Figs. 9 (a) and (b) show the comparison of the segmentation accuracy of different SR segmentation methods on DMR-IR and DBT-TU-JU databases respectively. Table-II demonstrates the average, maximum, and minimum of the accuracies of different methods for both the databases, where the best result is shown in bold font. The results, shown in both the Figure and Table, indicate that the proposed method notably retained better accuracy than the three state-of-the-art methods for the segmentation of the SRs. Also, the minimum obtained accuracy of the proposed method is significantly higher for both the databases than the other methods.

However, the segmentation accuracy (23) as computed earlier, alone is not sufficient to quantitatively evaluate the quality of the segmentation results. Because one method may under- or over-segment the SRs, which are also needed to measure quantitatively in order to quantify the quality of the segmentation results. Therefore, to evaluate the segmentation results more accurately, we have used the following kinds of metrics: area overlapping similarity (AOS) measure [31], and area error (AE) measure [32]. The most popularly used AOS measures are Dice Similarity (DS) [31], and Tanimoto (TN) [31]. These metrics compute the ratio of intersecting and non-intersecting regions of the segmented image and ground-truth. The score of these metrics varies in the range 0 to 1, with 1 signifies a perfect match between the segmentation results and ground-truths [31]. In the case of TBI analysis, where the diagnostic decision is extremely dependent on the accurate segmentation of the SRs, it is always desirable to have high values for all these metrics. Given a segmented image  $p_b^s$  obtained by the proposed method and the corresponding ground-truth image  $gt$ , the DS and TN are computed as [31]  $DS = 2|p_b^s \cap gt|/|p_b^s| + |gt|$

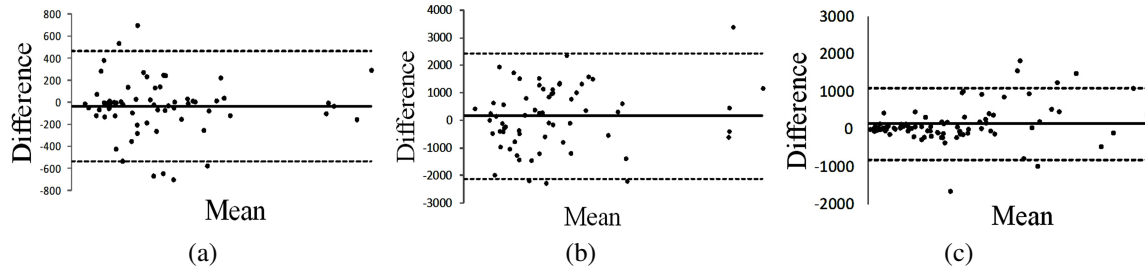


Figure 7. The Bland-Altman plots (a) inter-expert agreement on ground-truths of DMR-IR database, (b) area segmented by PM vs. *gt* of DMR-IR database, and (c) area segmented by PM vs. ground-truth of DBT-TU-JU database.

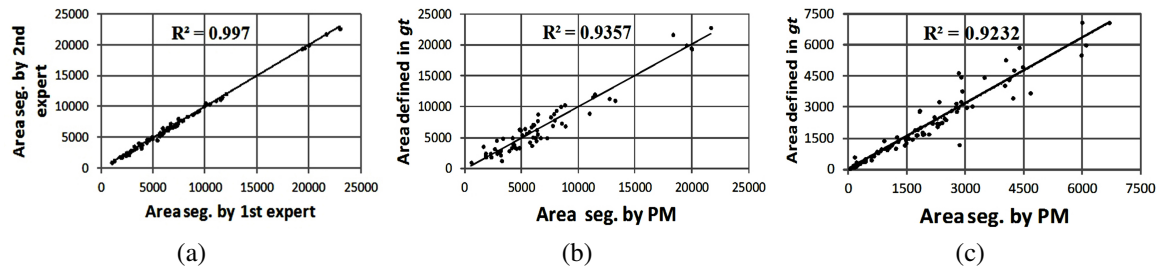


Figure 8. The linear regression plots (a) inter-expert agreement on ground-truths of DMR-IR database, (b) area segmented by PM vs. *gt* of DMR-IR database, and (c) area segmented by PM vs. ground-truth of DBT-TU-JU database.

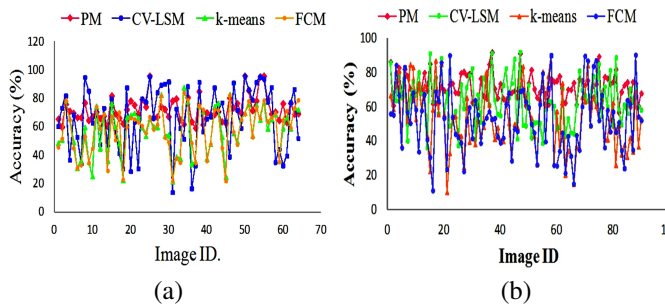


Figure 9. Comparison of the segmentation accuracies of PM, CV-LSM, k-means, and FCM for all the test images of (a) DMR-IR and (b) DBT-TU-JU databases.

and  $TN = (\overline{|p_b^s \cap gt|} + \overline{|p_b^s \cup gt|}) / (\overline{|p_b^s \cup gt|} + \overline{|p_b^s \cap gt|})$  respectively.

Besides, two most accepted area error (AE) metrics such as true positive (TP) area ratio and false positive (FP) area ratio [32] are also used to validate the segmentation results of PM. These measures typically evaluate how much of the SR is correctly segmented by PM and how much is erroneously segmented. A high *TP*-score indicates that the PM segments maximum of the SRs. Besides, a low *FP*-score indicates less erroneous segmentation of the non-suspicious region. Therefore, for a robust segmentation method, it is always desirable to have high *TP*-score and low *FP*-score. The *TP* and *FP* are computed as  $TP = |gt \cap p_b^s| / |gt|$  and  $FP = |(gt \cup p_b^s) - gt| / |gt|$  [32].

Table-III shows the means and variances of DS, TN, TP, and FP-ratio scores of PM, and three different state-of-the-art SR segmentation methods mentioned earlier. These results demonstrate that PM consistently retained significant improvement over the other methods for both DMR-IR and DBT-TU-JU databases. The average DS and TN-scores of

PM for both the databases are found to be 0.802, 0.780, and 0.968, 0.979 respectively, which are significantly higher than those of the other methods listed in Table-III. Also, the low variances of DS and TN-scores indicate the stability of PM for the segmentation of the SRs. In contrast, the variances of DS and TN-scores of CV-LSM, k-means, and FCM are very high which in turn indicates that the segmentation results obtained by these methods are not consistent. From Table-III, it is also observed that the average TP and FP-ratio scores of k-means and FCM methods for both the databases have occupied the leading positions. This means that the k-means and FCM methods segmented a lot of non-SRs along with the SRs. Besides, the TP-ratio scores of PM on DMR-IR and DBT-TU-JU databases are 0.862 and 0.844 respectively, which signify that PM effectively segments the SRs considerably well. Likewise, the FP-ratio scores of PM on the two databases are 0.168 and 0.145, which are considerably low and indicate very less amount of non-SRs are segmented by PM compared to the other methods. It can also be seen that there are very low variances of TP and FP-ratio scores of PM for both the databases. These results ensure that the segmentation results of PM are accurate, consistent, and credible compared to the segmentation results of the other methods listed in Table-III.

We have also conducted an experiment to illustrate the contribution of the proposed SCH-CS method and different local priorities embedded (DLPE) level set formulation in segmenting SRs. In this experiment, the DLPE-based level set method is compared with the conventional local region-based active contour model (local Chan-Vese level set method (LCV-LSM) [34]) for both manual initialization and SCH-CS-based initialization. Fig. 10 demonstrates some results of this experiment. From the Fig.10, it can be concluded that our proposed DLPE-based level set method with SCH-CS-based initialization scheme shows significantly high performance in

Table III  
SEGMENTATION RESULTS COMPARISON FOR BOTH THE DATABASES.

Databases	Methods	DS		TN		TP		FP	
		Mean	Var.	Mean	Var.	Mean	Var.	Mean	Var.
DMR-IR Database	PM	<b>0.802</b>	<b>0.004</b>	<b>0.968</b>	<b>0.0002</b>	0.862	<b>0.005</b>	<b>0.168</b>	<b>0.018</b>
	CV-LSM[10]	0.772	0.033	0.964	0.0016	0.838	0.031	0.492	1.075
	k-means[7]	0.721	0.020	0.948	0.0008	0.959	0.005	0.838	0.581
	FCM[7]	0.713	0.021	0.947	0.0008	<b>0.960</b>	0.005	0.867	0.550
DBT-TU-JU Database	PM	<b>0.780</b>	<b>0.004</b>	<b>0.979</b>	<b>0.0002</b>	0.844	<b>0.008</b>	<b>0.145</b>	<b>0.010</b>
	CV-LSM[10]	0.673	0.042	0.979	0.0007	0.813	0.071	1.041	2.371
	k-means[7]	0.655	0.035	0.974	0.0007	<b>0.934</b>	0.032	1.257	2.526
	FCM[7]	0.648	0.038	0.974	0.0006	0.920	0.044	1.208	2.354

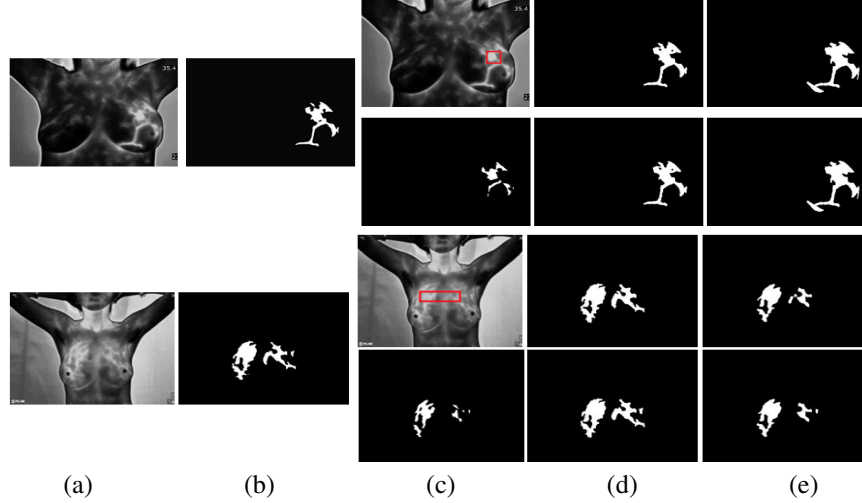


Figure 10. Impact of SCH-CS and proposed DLPE based LSM (PM) on the segmentation of the SRs:(a) grayscale images of DMR-IR and DBT-TU-JU databases, (b) ground-truths, (c) initialization (1st row and 3rd row: manually initialized square inside the SR; 2nd row and 4th row: our SCH-CS based initialization technique), (d) segmentation result obtained by the PM (1st row: ET 18.127s, Iterations 560, DS 0.893, TN 0.988, TP 1.000, FP 0.239; 2nd row: ET 7.285s, Iterations 210, DS 0.893, TN 0.988, TP 1.000, FP 0.239; 3rd row: ET 13.381s, Iterations 460, DS 0.910, TN 0.985, TP 0.980, FP 0.172; 4th row: ET 8.916s, Iterations 380, DS 0.929, TN 0.989, TP 0.990, FP 0.140), and (e) segmentation results obtained by the LCV-LSM (1st row: ET 28.070s, Iterations 830, DS 0.752, TN 0.971, TP 0.986, FP 0.636; 2nd row: ET 7.319s, Iterations 220, DS 0.752, TN 0.971, TP 0.986, FP 0.636; 3rd row: ET 17.352s, Iterations 490, DS 0.880, TN 0.984, TP 0.787, FP 0.001; 4th row: ET 11.984s, Iterations 450, DS 0.855, TN 0.981, TP 0.748, FP 0.001).

segmenting SRs compared to the LCV-LSM using the same initialization regarding execution time (ET), iterations, DS, TN, TP, and FP measures.

In Fig. 11, we qualitatively compared our segmentation results with the ground-truths, and three state-of-the-art SR segmentation methods CV-LSM [13], k-means [11], and FCM [11], respectively. For the sake of fair comparison, all these methods are implemented according to the description mentioned in the respective papers. We have included segmentation results for four images of DMR-IR and DBT-TU-JU databases in which shape of SRs varies. First and second columns in Fig. 11 show the grayscale images and corresponding ground-truth segmentation results. The third column shows the segmentation results of PM. Fourth, fifth, and sixth columns illustrate the segmentation results of CV-LSM, k-means, and FCM, respectively. The TBIs in the first and second rows (collected from DMR-IR database), contains SRs in one and both breasts respectively. By comparing the segmentation results of PM with the ground-truths, it can be observed that PM segments the SRs almost in exact shape. In contrast, CV-LSM misses some of the SRs, while k-means and FCM segment the SRs along with some portion of the background tissue regions. Besides, for the images in the third and fourth rows (collected from DBT-TU-JU database), CV-LSM, k-means, and FCM

segmented the SRs along with significant amount of non-SRs, whereas, PM precisely segments the SRs. It must be noted that the k-means and FCM have produced under-segmentation results for all the images in Fig. 11 whereas CV-LSM has produced very inconsistent segmentation results. Therefore, from the above discussion, it can be concluded that PM has potential to produce satisfactory segmentation results, even when images are blurred, as shown in the images of the first and second rows of Fig. 11.

However, in a few cases, the proposed method fails to segment the SRs accurately. Fig. 12 shows some failure cases. Typically, when the SR and the other hot regions are very close to each other, and their boundaries are indistinct, the proposed method may produce unsatisfactory segmentation results. Hence, in our future work, we will try to resolve this issue by incorporating local multi-scale analysis of each pixel in the level set formulation.

### C. Experiment 2: Differentiation of abnormal and normal breast thermograms

In this section, the effectiveness of the proposed STBIA system in the diagnostic differentiation of thermal breast images into normal and abnormal classes is studied. As discussed in section-III, after segmentation of the SRs, 21-elements

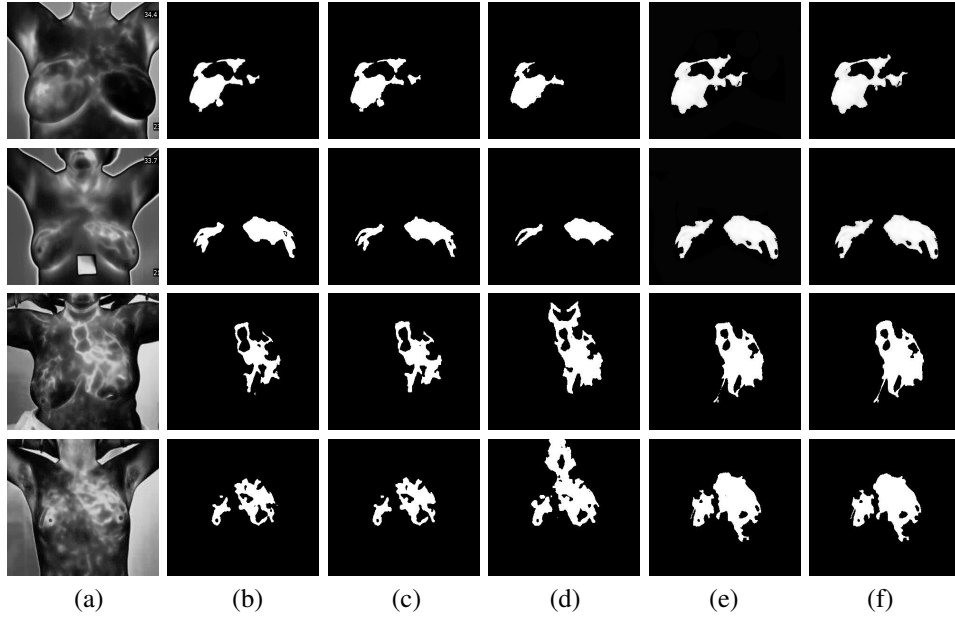


Figure 11. Comparison of the segmentation results. (a) grayscale images, (b) ground-truths, (c-f) segmentation results of PM, CV-LSM, k-means, and FCM respectively.

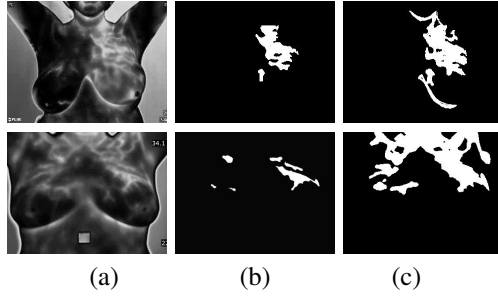


Figure 12. Some failure cases. (a) grayscale images, (b) ground-truths, (c) results obtained by the proposed method.

asymmetry feature vector is formed for each patient's breast thermogram, which is then fed to the FANN [23] for the classification purpose. A 5-fold cross-validation technique is used in this work to evaluate the performance of the proposed STBIA system. In each fold, 124 breast thermograms (72 normal and 52 abnormal) are used for training purpose whereas 31 breast thermograms (18 normal and 13 abnormal) are used for testing purpose. Different performance metrics like, accuracy, sensitivity, specificity, positive predictive value (PPV), and negative predictive value (NPV) [3] are used to evaluate the performance of the classifier. Table-IV summarizes the average percentage of all these metrics. Additionally, to quantify the efficacy of the proposed STBIA system over other systems for breast abnormality detection from TBIs, we have compared STBIA system with two state-of-the-art breast cancer detection methods [35], [36], which focus on the whole TBI, without segmenting the SRs. In [35], firstly, the authors have converted the pseudo color breast thermogram into the equivalent grayscale image. After that, sixteen GLCM and run-length matrix based features are extracted from each of the manually cropped breast regions for asymmetry analysis. They validated their method on 50 breast thermograms collected from a

Table IV  
RESULTS COMPARISON OF THE PROPOSED STBIA AGAINST AM AND SM.

Methods	Sensitivity	Specificity	PPV	NPV	Accuracy	AUC
STBIA	<b>87</b>	89	<b>87</b>	<b>89</b>	<b>88.5</b>	<b>0.939</b>
AM [35]	18	<b>95</b>	77.7	56.5	58	0.542
SM [36]	36.5	83	65.8	59	60.9	0.596

private database. Besides, the authors in [36], have extracted seven GLCM- and five histogram-based features from each of the automatically segmented breast region to predict the breast abnormality. However, they have used total 80 frontal view breast thermograms of DMR-IR database to validate their system. In this work, for the sake of fair comparison, we have implemented these methods on our database, and compared the results with our STBIA system. Table-IV summarizes the comparison results of STBIA, Acharya method (AM) [35], and Sathish method (SM) [36]. As shown, it can be observed that the proposed STBIA can identify the abnormal thermal breast images (sensitivity of 87%) significantly well compared to the AM and SM (sensitivity of 18% and 36.5% respectively). Note that the images, used in this work, have a tiny difference between the abnormal and normal cases. Therefore, for these types of images, 88.5% accuracy obtained by the proposed STBIA method is highly clinically significant for the diagnostic classification of the breast thermograms into abnormal and normal cases.

## V. CONCLUSION

Accurate segmentation of the suspicious regions (SRs) from thermal breast images is crucially important for the diagnosis of the breast cancer. However, it is an arduous task that requires a high degree of accuracy. In this work, therefore, we have proposed a novel region-based active contour model to precisely segment the SRs. A novel adaptive threshold-

ing technique, i.e., smaller-peaks corresponding to the high-intensity-pixels and the centroid-knowledge of suspicious-regions (SCH-CS), is proposed to handle the improper initialization of the level set function effectively, and also used to adaptively estimate some controlling parameters of the proposed level set method. Moreover, we have formulated a new energy functional, called different local priorities embedded (DLPE) energy functional, which is then minimized using interleaved operation of the LSF to precisely segment the suspicious regions. The proposed DLPE energy functional can effectively handle the severe intensity nonuniformity which is very common in breast thermograms. Further, to numerically stop the level set function, a new stopping criterion is proposed. Finally, a suspicious-regions-based thermal breast image analysis (STBIA) system is proposed in this paper. The proposed SR segmentation method is evaluated on DMR-IR and DBT-TU-JU databases and the average segmentation accuracies obtained on these databases are 72.18% and 71.26% respectively. These results confirm the superiority of our proposed segmentation method in segmenting the SRs over the other state-of-the-art SR segmentation methods. Also, our proposed STBIA system achieved an overall accuracy of 88.5% in differentiating the abnormal breast from the normal one, which is better than other existing methods. In the future, we will try to develop more precise energy functional to segment the SRs more accurately.

## REFERENCES

- [1] S. Pramanik, M. K. Bhowmik, D. Bhattacharjee, M. Nasipuri, "Hybrid Intelligent Techniques for Segmentation of Breast Thermograms," *Hybrid Soft Computing for Image Segmentation*, Springer, 255-289, 2016.
- [2] K. R. Foster, "Thermographic detection of breast cancer," *IEEE Engineering in Medicine and Biology*, 17, 10-14, 1998.
- [3] T. B. Borchart, A. Conci, R. C. F. Lima, R. Resmini, A. Sanchez, "Breast thermography from an image processing viewpoint: A survey," *Signal Processing*, 93, 2785-2803, 2013.
- [4] E. Gerasimova, B. Audit, S. G. Roux, A. Khalil, F. Argoul, O. Naimark, A. Arneodo, Multifractal analysis of dynamic infrared imaging of breast cancer, *EPL (Europhysics Letters)*, 104(6), 2014, 68001.
- [5] E. Gerasimova, B. Audit, S. G. Roux, A. Khalil, O. Gileva, F. Argoul, O. Naimark, A. Arneodo, Wavelet-based multifractal analysis of dynamic infrared thermograms to assist in early breast cancer diagnosis, *Frontiers in physiology*, 5, 176, 2014.
- [6] E. Gerasimova, B. Toner, Z. Marin, B. Audit, S. G. Roux, F. Argoul, A. Khalil, O. Gileva, O. Naimark, A. Arneodo, Comparative multifractal analysis of dynamic infrared thermograms and X-Ray mammograms enlightens changes in the environment of malignant tumors, *Frontiers in physiology*, 7, 336, 2016.
- [7] A. Arneodo, N. Decoster, P. Kestener, S. G. Roux, A wavelet-based method for multifractal image analysis: from theoretical concepts to experimental applications, In *Advances in imaging and electron physics*, 126 (2003), 1-92.
- [8] R. Mulaveesala, G. Dua, Non-invasive and non-ionizing depth resolved infra-red imaging for detection and evaluation of breast cancer: a numerical study, *Biomedical Physics and Engineering Express*, 2(5), 2016, 055004.
- [9] G. Dua, R. Mulaveesala, Applicability of active infrared thermography for screening of human breast: a numerical study, *Journal of biomedical optics*, 23(3), 2018, 037001.
- [10] M. EtehadTavakol, V. Chandran, E. Y. K. Ng, R. Kafieh, "Breast cancer detection from thermal images using bispectral invariant features," *International Journal of Thermal Sciences*, 69, 21-36, 2013.
- [11] M. EtehadTavakol, S. Sadri, E. Y. K. Ng, "Application of K- and fuzzy c-means for color segmentation of thermal infrared breast images," *Journal of Medical Systems*, 34, 35-42, 2010.
- [12] M. Milosevic, D. Jankovic, A. Peulic, "Thermography based breast cancer detection using texture features and minimum variance quantization," *EXCLI Journal*, 13, 1204-1215, 2014.
- [13] N. Golestani, M. EtehadTavakol, E. Y. K. Ng, "Level set method for segmentation of infrared breast thermograms," *EXCLI Journal*, 13, 241-251, 2014.
- [14] M. EtehadTavakol, E. Y. K. Ng, "Color Segmentation of Breast Thermograms: A Comparative Study," in *Application of Infrared to Biomedical Sciences*, Springer Singapore, 69-77, 2017.
- [15] T. F. Chan, L. A. Vese, "Active contours without edges," *IEEE Trans. Image Process.* 10(2), 266277, 2001.
- [16] C. Li, C. Xu, C. F. Gui, M. D. Fox, "Distance Regularized Level Set Evolution and Its Application to Image Segmentation," *IEEE Trans. on Image Processing*, 19 (12), 3243-3254, 2010.
- [17] C. Liu, W. Liu, W. Xing, "An improved edge-based level set method combining local regional fitting information for noisy image segmentation," *Signal Processing*, 130 (2017), 12-21, 2017.
- [18] C. Li C. Y. Kao, J. C. Gore, Z. Ding, "Minimization of region-scalable fitting energy for image segmentation," *IEEE Trans. on Image Processing*, 17(10), 1940-1949, 2008.
- [19] X. F. Wang, H. Min, L. Zou, Y. G. Zhang, "A novel level set method for image segmentation by incorporating local statistical analysis and global similarity measurement," *Pattern Recognition*, 48(2015), 189-204, 2015.
- [20] S. Osher, R. Fedkiw, "Level Set Methods and Dynamic Implicit Surfaces," 153, Springer-Verlag New York, Inc., 2003.
- [21] S. Pramanik, D. Bhattacharjee, M. Nasipuri, "Wavelet based thermogram analysis for breast cancer detection," In *IEEE ISACC*, 205-212, 2015.
- [22] <http://www.andrews.edu/calkins/math/edrm611/edrm03.htm> (last accessed 12/8/2017)
- [23] D. Bhattacharjee, A. Seal, S. Ganguly, M. Nasipuri, D. K. Basu, "A Comparative Study of Human Thermal Face Recognition Based on Haar Wavelet Transform and Local Binary Pattern," *Computational Intelligence and Neuroscience*, 2012, 1-12, 2012.
- [24] U. Vovk, F. Pernus, and B. Likar, "A Review of Methods for Correction of Intensity Inhomogeneity in MRI," *IEEE Trans. on Medical Imaging*, 26(3), 405-421, 2007.
- [25] X. F. Wang, H. Min, and Y. G. Zhang, "Multi-scale local region based level set method for image segmentation in the presence of intensity Inhomogeneity," *Neurocomputing*, 151(2015), 1086-1098, 2015.
- [26] A. Banerjee, and P. Maji, "Rough Sets for Bias Field Correction in MR Images Using Contraharmonic Mean and Quantitative Index," *IEEE Trans. on Medical Imaging*, 32(11), 2140-2151, 2013.
- [27] S. Osher, J. Sethian, "Fronts propagation with curvature-dependent speed: algorithms based on Hamilton-Jacobi formulations," *J. Comput. Phys.*, 79, 12-49, 1988.
- [28] R. Haralick, K. Shanmugam, I. Dinstein, "Textural Features for Image Classification," *IEEE Trans Syst Man Cybern*, 3(6), 610621, 1973.
- [29] H. Ming-Kuei, "Visual pattern recognition by moment invariants," *IRE Transactions Information Theory*, 8, 179-187, 1962.
- [30] L. F. Silva, D. C. M. Saade, G. O. Sequeiros-Olivera, A. C. Silva, A. C. Paiva, R. S. Bravo, A. Conci, "A New Database for Breast Research with Infrared Image," *J. Med. Imaging Health Inf.*, 4(1), 92-100, 2014.
- [31] R. Cardemes, L. G. Rd, M. B. Cuadra, "A multi-dimensional segmentation evaluation for medical image data," *Computer Methods and Programs in Biomedicine*, 96(2009), 108124, 2009.
- [32] A. Madabhushi, D. N. Metaxas, "Combining low-, high-level and empirical domain knowledge for automated segmentation of ultrasonic breast lesions," *IEEE Trans. on Med. Imaging*, 22, 2(2003), 155-169, 2003.
- [33] M. K. Bhowmik, U. R. Gogoi, G. Majumdar, D. Bhattacharjee, D. Datta, A. K. Ghosh, Designing of Ground Truth Annotated DBT-TU-JU Breast Thermogram Database towards Early Abnormality Prediction, *IEEE journal of biomedical and health informatics*, 2017 (article in Press).
- [34] X. F. Wang, D. S. Huang, H. Xu, "An efficient local ChanVese model for image segmentation," *Pattern Recognition*, 43(3), 603-618, 2010.
- [35] U. R. Acharya, E. Y. K. Ng, J. H. Tan, S. V. Sree, Thermography based breast cancer detection using texture features and support vector machine, *Journal of medical systems*, 36(3), 1503-1510, 2012.
- [36] D. Sathish, S. Kamath, K. Prasad, R. Kadavigere, R. J. Martis, Asymmetry analysis of breast thermograms using automated segmentation and texture features, *Sig., Img. and Vid. Processing*, 11(4), 745-752, 2017